Journal of Applied Physics ARTICLE pubs.aip.org/aip/jap

Two surface multipactor with non-sinusoidal RF fields

Cite as: J. Appl. Phys. **134**, 153304 (2023); doi: 10.1063/5.0170070
Submitted: 31 July 2023 · Accepted: 25 September 2023 ·
Published Online: 18 October 2023

Asif Iqbal,[1,a)] De-Qi Wen,[1,2] John Verboncoeur,[1,2] and Peng Zhang[1,a)]

AFFILIATIONS

[1]Department of Electrical and Computer Engineering, Michigan State University, East Lansing, Michigan 48824-1226, USA
[2]Department of Computational Mathematics, Science, and Engineering, Michigan State University, East Lansing, Michigan 48824-1226, USA

[a)]**Authors to whom correspondence should be addressed:** iqbalas3@msu.edu and pz@egr.msu.edu

ABSTRACT

Two-surface multipactor with a Gaussian-type waveform of rf electric fields is investigated by employing Monte Carlo simulations and 3D electromagnetic particle-in-cell simulations. The effects of the full width at half maximum (FWHM) of the Gaussian profile on multipactor susceptibility and the time dependent dynamics are studied. The threshold peak rf voltage, as well as the threshold time-averaged rf power per unit area for multipactor development, increases with a Gaussian-type electric field compared to that with a sinusoidal electric field. The threshold peak rf voltage and rf power for multipactor susceptibility increase as the FWHM of the Gaussian profile decreases. Compared to sinusoidal RF operation, the expansion of multipactor susceptibility bands is observed. In the presence of space charge, a high initial seed current density can shrink the multipactor susceptibility bands. The effect of space charge on multipactor susceptibility decreases as the FWHM of the Gaussian profile decreases. Decreasing the FWHM of the Gaussian electric field can reduce the electron population corresponding to the strength of the multipactor at saturation, at fixed time-averaged input power.

I. INTRODUCTION

Multipactor[1–6] is a nonlinear discharge phenomenon, which is generally considered undesirable as it can be detrimental to a multitude radio frequency (rf) and microwave devices, such as high power microwave sources,[7] particle accelerators,[8–10] traveling wave tubes (TWTs),[11] satellite communication payloads and spacecraft components,[12–14] and fusion systems.[15] Problems caused by multipactor include the breakdown of dielectric windows,[16–19] erosion of metallic structures, melting of internal components, and perforation of vacuum walls.[2] In addition, multipactor can often detune rf systems, cause multi-tone coupling and signal distortion,[20] limit the transmission or delivery of rf power, and cause a local pressure rise due to the desorption of surface gases.[21]

A common manifestation of multipactor discharge is an electron avalanche created between two metal electrodes separated by a vacuum gap and exposed to a radio frequency electric field.[2] Under favorable conditions,[2,22] electrons can be locked into a resonant motion in such a two-surface geometry and cause a rapid charge growth through secondary electron emission[23–26] by repeatedly impacting the parallel electrodes. Such an electron avalanche may lead to the cutoff of the power transmission or damage of an rf device.[27] It should be noted that multipactor can be manifested in a single-surface geometry as well where a rapid charge growth through secondary electron emission can occur without electrons being locked into resonant motion.[3,6,28–31]

Mitigation of multipactor has been one of the major challenges for the RF community over the past few decades. Common methods employed for multipactor mitigation include device and surface engineering, such as coating the surfaces with materials having low secondary electron yield (SEY)[32–38] and using artificially roughened, grooved, and porous surfaces with low effective SEY[39–49]. These methods, albeit effective, can be challenging to implement in components that are already in use in various applications.[22] In addition, system geometries may have engineering constraints or may be fixed by the necessary boundary conditions as in a waveguide, which calls for the employment of other methods to prevent multipactor.

To address this limitation, in recent years, great emphasis has been put on multipactor mitigation techniques that modify the electric or magnetic fields. In addition to the well-known methods such as applying an external dc electric[50,51] or magnetic[52–54] field, recent studies have focused on engineering the rf field. Iqbal *et al.* studied multipactor mitigation using two-frequency rf fields in both single- and two-surface geometries.[30,55–59] In a two-surface geometry, the modulation of the rf envelope due to multiple carrier frequencies leads to the disruption of the resonant electron motion, resulting in multipactor mitigation.[8,60] Wen *et al.* showed[27,61] that electric fields consisting of several frequency components, such as the non-sinusoidal Gaussian-type rf fields, can be very effective for single-surface multipactor mitigation (reduced the multipactor strength by an order of magnitude compared to sinusoidal rf operation for the same transmission rf power).[27,61] In practical vacuum devices, such waveforms could be generated by superimposing multiple sinusoidal signals with different carrier frequencies and phase shifts for engineering purposes.[27,62] Wen *et al.* showed[27] that single-surface multipactor mitigation can be obtained with an approximate Gaussian-type rf field generated by superimposing as few as three sinusoidal signals. Multipactor mitigation due to the oblique incidence of the rf fields[63] has also been studied.

In this article, we investigate two surface multipactor with non-sinusoidal Gaussian-type rf electric fields using Monte Carlo (MC) simulation and particle-in-cell (PIC) simulations using Computer Simulation Technology (CST) Particle Studio. We characterize the effect of the full width at half maximum (and/or half minimum) (FWHM) of the Gaussian profile on multipactor susceptibility and time dependent physics. We also investigate the effect of space charge[59,64–67] in two surface multipactor with Gaussian rf waveform. It is noteworthy that the study in Ref. 59 is focused on engineering the rf waveform with a two-frequency sinusoidal signal, whereas the current study focuses on the Gaussian-type signal, which intrinsically comprises an infinite number of carrier frequencies, while for practical purposes, it can be recovered by superimposing several carrier frequency sinusoidal signals.[63]

We start with a brief introduction to the electron dynamics and the force law in Sec. II. Section III presents the MC simulation and CST PIC model.[68] The results of our study are presented in Sec. IV. A summary with the main conclusions and possible future work are presented in Sec. V.

II. THE FORCE LAW

Figure 1 depicts a simplified schematic of two surface planar multipactor neglecting space charge with a Gaussian-type rf electric field,[27]

$$E_y(t) = \frac{V_{rf}}{d} \times \{\exp[-\beta(t-t_1)^2] - \exp[-\beta(t-t_2)^2]\}, \quad nT_{rf} \le t < (n+1)T_{rf}, \tag{1}$$

where V_{rf} is the peak of the applied RF voltage, d is the distance between the parallel plates A and B, and $t_1 = (n+0.25)T_{rf}$ and

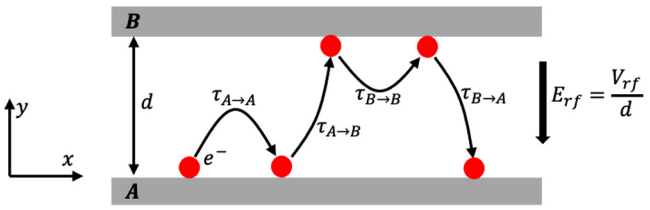

FIG. 1. Multipactor discharge with an electric field oscillating between two metal electrodes A and B separated by a gap distance d.[59] Here, $\tau_{A\to A}$, $\tau_{A\to B}$, $\tau_{B\to A}$, and $\tau_{B\to B}$ represent a particle's transit times from electrode A to A, electrode A to B, electrode B to B, and electrode B to A, respectively. Therefore, $\tau_{A\to A}$ and $\tau_{B\to B}$ correspond to single-surface impacts, whereas $\tau_{A\to B}$ and $\tau_{B\to A}$ correspond to two-surface impacts.

$t_2 = (n+0.75)T_{rf}$ are the time for RF field maximum and minimum, respectively, with n being an integer and T_{rf} being the repetition period. The FWHM of the Gaussian wave can be expressed in terms of the shape-controlling parameter (β) as $\Delta\tau = 2\sqrt{\ln 2/\beta}$. Figure 2 shows the temporal profiles of sinusoidal and Gaussian-type electric fields with different FWHMs but the same time-averaged rf power per unit area, $P_{rf} = \frac{c\epsilon_0}{T_{rf}}\int_0^{T_{rf}} |E_y(t)|^2 dt$, where c is the speed of light and ϵ_0 is the vacuum permittivity. Therefore, a smaller FWHM value (Δτ) corresponds to a sharper and larger peak of the Gaussian-type rf field.

Assuming one-dimensional particle motion along the y-direction, the force law governing the electron trajectories is as

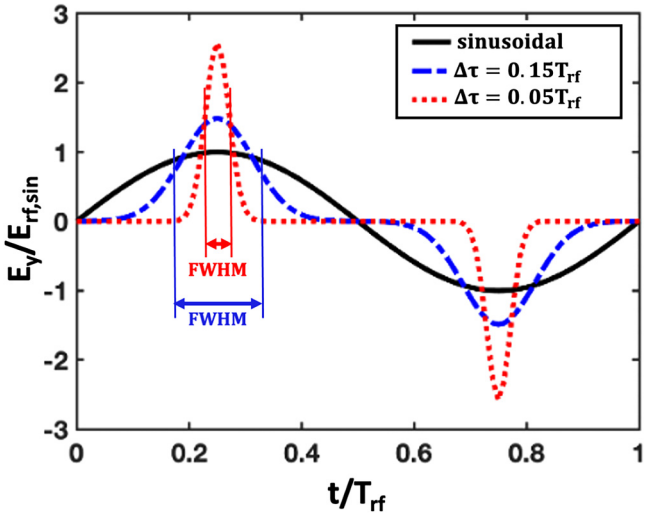

FIG. 2. The instantaneous electric field (neglecting space charge) of the sinusoidal (solid black curve) and Gaussian form for FWHM, $\Delta\tau = 0.15T_{rf}$ (dashed blue curve) and $0.05T_{rf}$ (dotted red curve). All fields correspond to a time-averaged RF power per unit area, $P_{rf} = \frac{c\epsilon_0}{T_{rf}}\int_0^{T_{rf}} |E_y(t)|^2 dt = c\epsilon_0 \frac{E_{rf,sin}^2}{2}$ (W/m²).

follows:

$$a_y(t) = \frac{eE_y(t)}{m}, \tag{2}$$

where $a_y(t)$ is the acceleration. The instantaneous velocity of the electron is obtained as

$$v_y(t) = \int_0^t a_y(t)dt + v_0, \tag{3}$$

and the instantaneous position of a multipactor electron along the y-direction is obtained as

$$y(t) = \int_0^t v_y(t)dt + v_0 t + y_0. \tag{4}$$

Here, y_0 is the initial position of the electron at $t = 0$ and v_0 is the initial velocity of the electron.

III. METHODS

In the current work, we separately applied MC and PIC simulations to investigate the multipactor discharge on the two-surface configuration. A brief description of these methods is provided below.

A. Monte Carlo simulation

To calculate the growth rate of the multipactor discharge, we follow the trajectory of a weighted macroparticle over a large number of impacts in a 1D2V (i.e., assuming one-dimensional particle trajectory in space and two components of the particle velocity) MC simulation,[3,29,31] neglecting space charge effects in both volume and the surface charges induced by the volume charges. The initial rf phase (t/T_{rf}) is uniformly distributed over a complete rf period. Each time a macroparticle leaves the surface of an electrode, we assign it a random initial energy $V_0 = (1/2)mv_o^2$ and angle ϕ (with respect to the surface tangent, representing an isotropic flux) according to the following distributions:[28]

$$f(V_0) = \frac{V_0}{V_{0m}^2} e^{-\left(\frac{V_0}{V_{0m}}\right)}, \tag{5a}$$

$$g(\phi) = \frac{1}{2}\sin\phi, \quad 0 < \phi < \pi. \tag{5b}$$

where V_{0m} is the peak of the distribution of emission energies.[28] In all MC simulations in this article, we choose $V_{0m} = 2$ eV. It is important to note that the value of v_0 is never known with accuracy,[2] and simulations using a statistical distribution such as Eq. (5) can only approximately represent the multipactor dynamics.[2] Transit times of an electron in flight for single- ($\tau_{A\to A}$, $\tau_{B\to B}$ in Fig. 1) and two-surface ($\tau_{A\to B}$, $\tau_{B\to A}$ in Fig. 1) impacts on the plates are calculated by solving Eq. (4). Then, we calculate the impact energy, $V_i = mv_i^2/2$, from Eq. (3) and the secondary electron yield, δ, from Vaughan's model.[25,69]

Upon each impact of a primary particle on the surface, we update the charge and mass on the macroparticle according to the SEY and then emit it again with a random velocity. We repeat the process to obtain a series of yields ($\delta_1 . \delta_2 \ldots \delta_N$) for N_i consecutive impacts. The geometric average value of secondary yield over N_i impacts is then calculated as $\delta_{avg} = (\delta_1 . \delta_2 \ldots \delta_{N_i})^{1/N_i}$, where $N_i = 20$ is used in the calculation.[59]

For a specific combination of rf frequency f (i.e., inverse of the waveform period), gap distance d, and accelerating voltage V_{rf}, if we find a valid electron trajectory for any of the initial rf phase, for which $\delta_{avg} > 1$, we conclude that multipactor discharge develops in the system for this set of parameters.

B. CST PIC model

We employ the three-dimensional electromagnetic PIC simulation setup described in Sec. III C in Ref. 59. Using two waveguide ports, which are perpendicular to the electrode surfaces, we apply a constant amplitude of $f = 1$ GHz excitation in a parallel plate geometry (see the schematic of the geometric setup for the simulation in Fig. 3 of Ref. 59). We apply the PEC (perfect electric conductor, i.e., tangential electric field, $E_t = 0$) boundary condition to the electrode surfaces as well as the waveguide ports and PMC (perfect magnetic conductor, i.e., tangential magnetic field, $H_t = 0$) boundary condition to the surfaces that are orthogonal to both the waveguide ports and the electrode surfaces. We use hexahedral meshes with space step sizes in the y- (normal to the electrode surfaces), x- (along the electrode length), and z- (along the electrode width) directions, $dy = d/10$, $dx = l/20$, and $dz = w/20$, respectively, where $l = 20$ and $w = 20$ mm are the length and width of the electrode surfaces, respectively, and d is the electrode separation (see Fig. 3 in Ref. 59). A variation in fd is realized in the simulation by varying the gap distance, d.

The inbuilt Vaughan's model of CST is used for secondary electron emission where the emission energy follows a gamma distribution weighted by a temperature, T_e, where $2T_e$ is the average emission energy of the secondary electrons.[68] In our simulations, we use $T_e = 2$ eV. Secondary electrons are emitted at angles relative to the surface normal with the following probability distribution function:[68]

$$f(\theta) = \cos\theta_N, \theta_N \in [0, \pi/2]. \tag{6}$$

Note that although Eq. (6) in CST documentation[68] has a different form compared to Eq. (5b), both equations represent an isotropic flux. We specify the super-particle weight (the number of physical particles represented by a computer particle), N_e, at the beginning of a simulation, which is kept fixed for all the particles throughout the simulation. A particle point source with an emission area of 10^{-4} mm^2 emits seed particles with an initial kinetic energy, $E_{k0} = 0$ eV, into the vacuum gap between the plates during the first period ($t_{emission} = 1$ ns) of the excitation at a constant rate of 1515 particles/ns (corresponding to an initial seed current density, $J_{seed} = 2.43 \times 10^8$ A/m^2 for $N_e = 10^5$) and remains inactive during the rest of the simulation.

With a time step of $\tau_s = 0.05$ ns (i.e., the time step width to monitor the particles in the simulation and collect parametric data,

not the step width of updating the electromagnetic fields in the PIC simulation, which is automatically set by the CST Particle Studio[68]), we run the simulation for t = 20 ns which corresponds to 20 cycles of the rf fields. The temporal evolution of secondary electron yield δ(t) is calculated as[70]

$$\delta(t) = \frac{n_e(t+\tau_s)}{n_e(t)}, \tag{7}$$

where $n_e(t)$ and $n_e(t+\tau_s)$ are the electron populations at time t and $(t+\tau_s)$, respectively. The time averaged value of δ(t) represents the average effective SEY of the simulation, δ_{avg}.[70]

Figure 3 shows the evolution of the electron population and the corresponding secondary electron yield at various gap voltage amplitudes of a sinusoidal rf field [corresponding to the susceptibility chart in Fig. 5(a)] for fd = 0.9902 GHz mm. We observe that for V_{rf} = 93 V (blue curves in Fig. 3), the average SEY δ_{avg} = 1.005 [Fig. 3(b)], and the corresponding electron population shows an exponential growth in Fig. 3(a). On the other hand, for V_{rf} = 111 V (red curves in Fig. 3), the average SEY δ_{avg} = 0.994 [Fig. 3(b)], and the corresponding electron population shows an approximate exponential decay in Fig. 3(a). For V_{rf} = 99 V, the average SEY is unity [black curves in Fig. 3]. In Fig. 3(a), the seed particle source is active during the first rf period ($t_{emission}$ = 1 ns) as discussed previously. Therefore, we observe a linear increase in the electron population at the beginning of the simulations [the inset in Fig. 3(a)] until seed particles reach the opposite plate at t ∼ 0.5 ns. Beyond the particle seeding period (i.e., t > 1 ns), only the particles satisfying the resonant condition[2,3] survive, while the rest of the particles die out. In Fig. 3(b), we show the SEY curves after the particle seeding period is over (i.e., t > 1 ns).

An important observation of Fig. 3(b) is the periodic variations in the SEY curves. To understand the reason for this, we recall that particles emitted from one surface reach the opposite surface in approximately one half of an rf period. As we observe from Fig. 4(a) (the same as the blue curve in Fig. 3(b), zoomed in at 4 ns ≤ t ≤ 5 ns), during 4.15 ns ≲t ≲4.3 ns, electron population and average SEY remain constant as particles emitted from the top plate traverse the gap distance toward the bottom plate. The front end of the particle bunch strikes the bottom plate at ∼4.3 ns [Fig. 4(c)]. These particles are highly energetic [impact energy ∼70 eV as shown in the red circled region in Fig. 4(c)] since they strike the bottom surface soon after the E-field reaches its peak. As the average impact energy is greater than the first crossover energy, E_1, of the SEY curve [Fig. 4(b)], the average SEY of these impacts is greater than unity [as observed in Fig. 4(a)]. The average SEY thereupon reaches a maximum value and then decreases during 4.4 ns < t < 4.5 ns. This is because during this period, in addition to some high energy impacts, many low-energy secondaries [impact energy < 10 eV as shown in the red circled region in Fig. 4(d)] are accelerated back by the electric field and absorbed at the bottom plate. The resultant average SEY during this period falls sharply below unity as seen in Fig. 4(a). During the negative half cycle of the E-field, electrons are accelerated toward the top plate and the pattern discussed above is repeated in the SEY curve [Fig. 4(a)] as particles impact the top plate.

IV. RESULTS AND DISCUSSION

Figure 5 shows the multipactor susceptibility charts calculated from MC simulations for random emission energy and isotropic angle following Eq. (5), and from CST simulations, for sinusoidal rf operation as well as Gaussian-type rf operation with FWHM $\Delta\tau = 0.15T_{rf}$ and $\Delta\tau = 0.05T_{rf}$. The difference between the MC

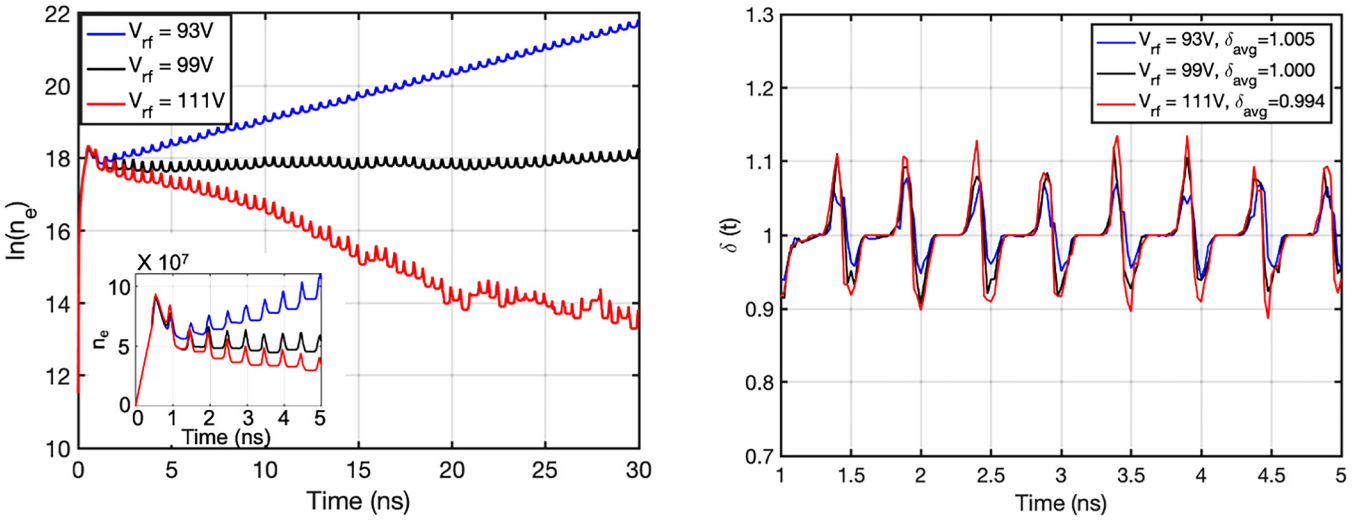

FIG. 3. (a) Exponential growth and decay of the electron population at various gap voltage amplitudes of a sinusoidal rf field [corresponding to the susceptibility chart in Fig. 5(a)]. (b) Evolution of the secondary electron yield δ(t) calculated from Eq. (7). These simulations were produced for sinusoidal RF operation with fd = 0.9902 GHz mm (f = 1 GHz, d = 0.9902 mm) using Vaughan's SEY model parameters for copper E_{max0} = 277.5 eV, δ_{max0} = 2.088.[59]

and CST results is due to the different simulation methodologies (chiefly the ability to populate phase space by emitting multiple particles per impact in CST) and secondary electrons' energy distribution functions adopted in the two models (see Sec. III of Ref. 59 for details). We observe that multipactor threshold voltage (i.e., the lower susceptibility boundary) increases with Gaussian-type RF waveshape [Fig. 5(b)] compared to the sinusoidal rf operation [Fig. 5(a)]. Figures 5(b) and 5(c) show that the threshold voltage increases further as the FWHM of the Gaussian profile decreases from $\Delta\tau = 0.15T_{rf}$ [Fig. 5(b)] to $\Delta\tau = 0.05T_{rf}$ [Fig. 5(c)]. This happens since for fixed peak rf voltage, as the FWHM decreases, the time-averaged rf power per unit area decreases and a higher peak rf voltage is required to provide enough energy to primary particles and generate secondaries.

Figures 5(d)–5(f) show that the threshold time averaged RF power per unit area P_{rf} for multipactor development also increases with a Gaussian-type RF waveshape [Fig. 5(e)] compared to a sinusoidal waveshape [Fig. 5(d)]. As the FWHM decreases, the threshold P_{rf} for multipactor development further increases [Fig. 5(f)]. This happens because for a fixed input RF power, as the width of the E-field pulse decreases with the Gaussian-type RF operation [i.e., $\Delta\tau = 0.05T_{rf}$ in Fig. 5(f)], the longer decay time between the Gaussian field peaks (cf. dotted red curve in Fig. 2) eliminates most free electrons.[6,27]

We also observe from Fig. 5 that susceptibility bands with the Gaussian-type rf waveshape are wider than those for sinusoidal rf operation. To explain this, we recall that for a sinusoidal rf electric field, $E_y = E_{rf}\sin(\omega t + \theta)$, each point of the upper multipactor boundary corresponds to the maximum negative value of the initial rf phase θ at that point, for which the emission velocity of an electron just allows it to escape against the initially retarding field.[2,3,6,21,22,69] This maximum negative value of the initial rf phase is shown in Fig. 6(a) as $\theta = -\theta_m$, which corresponds to the earliest electron emission time, $-t_{max,sin}$.

From Eq. (1), the slope of a Gaussian-type signal at any point in time can be expressed as

$$\frac{dE_y(t)}{dt} = \frac{V_{rf}}{d} \times \{\exp[-\beta(t-t_1)^2] \times [-2\beta(t-t_1)] - \exp[-\beta(t-t_2)^2] \times [-2\beta(t-t_2)]\}. \quad (8)$$

We find from Eqs. (1) and (8) that at the inflection point (i.e., $t_{inflection} = \frac{t_1+t_2}{2}$), $E_y(t_{inflection}) = 0$ and $\frac{dE_y(t)}{dt}|_{t=t_{inflection}} = 0$. On the other hand, for a sinusoidal signal [i.e., $E_{y,sin} = \frac{V_{rf}}{d}\sin(\omega t + \theta)$, where ω is the angular frequency, and θ is the initial phase of the electric field] at the inflection point, $E_{y,sin}(t_{inflection}) = 0$ and $\frac{dE_{y,sin}(t)}{dt}|_{t=t_{inflection}} = \frac{V_{rf}}{\omega d}\cos(\omega t + \theta)$. Therefore, for a Gaussian-type electric field, the rf field strength near the inflection point is lower compared to the sinusoidal electric field [the red elliptical region in Fig. 6(b)].

As a result, with a Gaussian-type electric field, an electron can survive being emitted earlier [$-t_{max,gauss} < -t_{max,sin}$ in Fig. 6(b)] during the negative half cycle compared to the sinusoidal rf operation, i.e., $|t_{max,gauss}| > |t_{max,sin}|$ (analogous to $\theta_{m,gauss} > \theta_{m,sin}$). Thus, a stronger peak rf voltage for the Gaussian-type rf waveshape has to be applied to bring the emitted electrons back to their birth electrode during the initial negative rf phase (in order to extinguish multipactor). This results in an increase in the upper susceptibility boundary and an expansion of the susceptibility bands. From another perspective, $\theta_{m,gauss} > \theta_{m,sin}$ signifies a larger range of the emission phase of secondary electrons with Gaussian-type rf fields that can establish a resonant motion compared to that with sinusoidal rf fields, resulting in the expansion of the susceptibility bands.

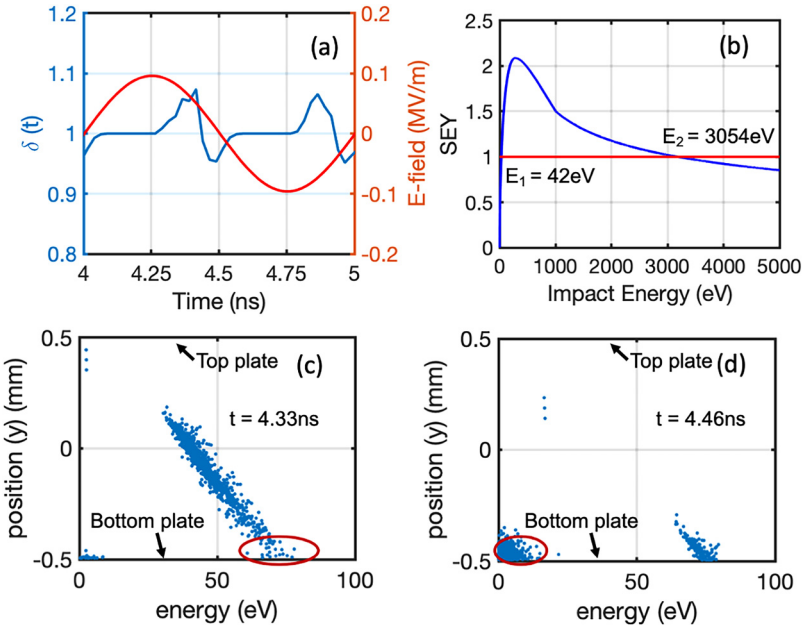

FIG. 4. Top row: (a) Secondary electron yield (blue curve) and electric field amplitude (red curve) for sinusoidal RF operation with fd = 0.9902 GHz mm (f = 1 GHz, d = 0.9902 mm), V_{rf} = 93 V; (b) Vaughan's SEY curve for copper with E_{max0} = 277.5 eV, δ_{max0} = 2.088.[59] The first and second crossover energies are E_1 = 42 eV and E_1 = 3054 eV, respectively. Bottom row: position (y) vs energy (E) phase-space plots at times (c) t = 4.33 ns, and (d) t = 4.46 ns. $y = 0.4951$ and -0.4951 correspond to the top plate and the bottom plate, respectively.

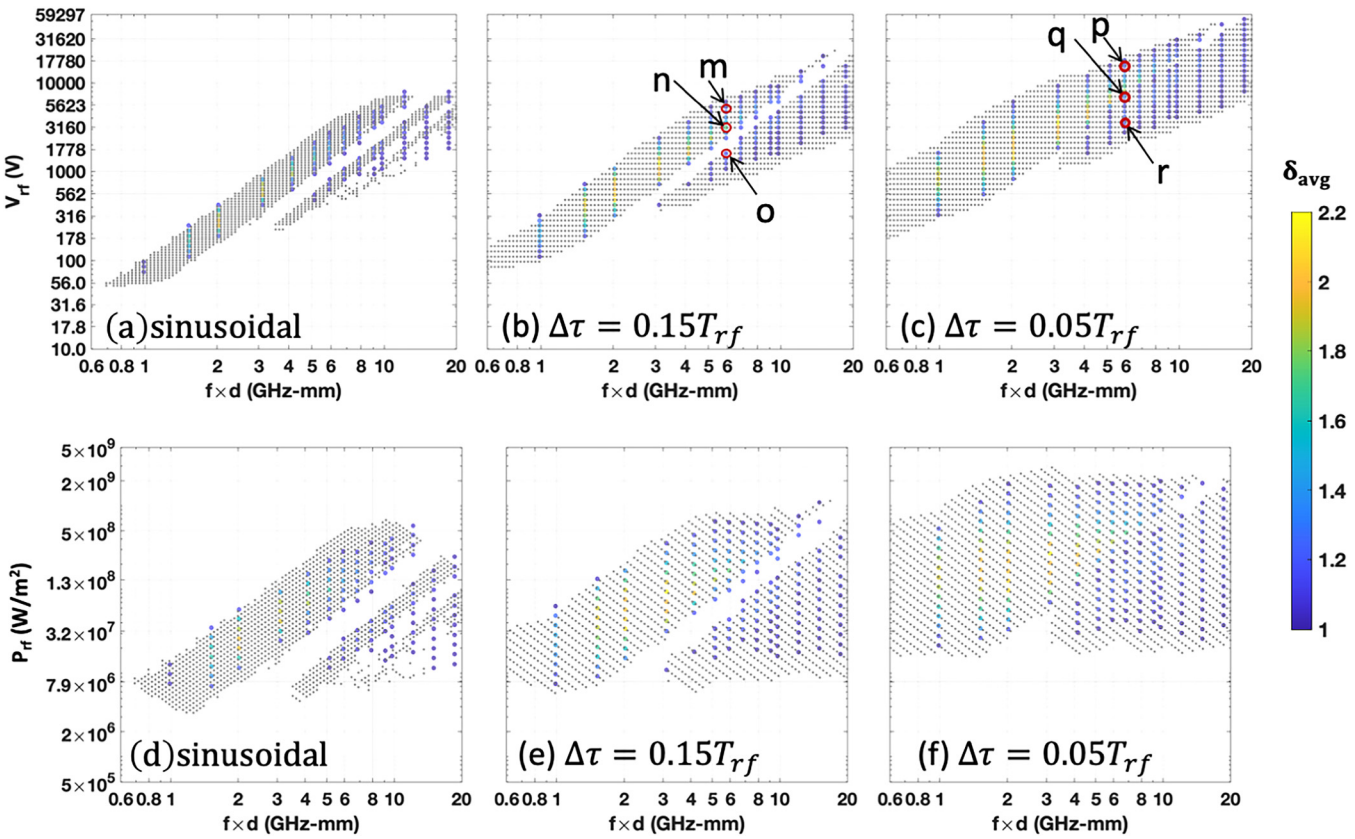

FIG. 5. Top row: Multipactor susceptibility charts in the $V_{rf} - fd$ space calculated from MC simulation (gray dots) for random emission energy and emission angle given by Eq. (5) and from CST simulation (colored dots) without space-charge effects for (a) sinusoidal rf operation, and Gaussian-type rf operations with (b) $\Delta\tau = 0.15T_{rf}$ and (c) $\Delta\tau = 0.05T_{rf}$. Bottom row: Susceptibility charts, the same as those in the top row, in the $P_{rf} - fd$ space. The time averaged rf power per unit area is calculated from $P_{rf} = \frac{\varepsilon_0}{T_{rf}} \int_0^{T_{rf}} |E_y(t)|^2 dt (W/m^2)$. The color bar shows the time averaged secondary electron yield, δ_{avg}, calculated from CST. For all the cases, we use rf repetition period, $T_{rf} = 1$ ns and variation in fd is obtained by varying the gap distance, d. For CST simulations, we use the number of electrons contained in each particle, $N_e = 10^5$, emission period of seed particles, $t_{emission} = 1$ ns and the total number of seed particles, $N_{seed,total} = 1515$ corresponding to an initial seed current density, $J_{seed} = 2.43 \times 10^8$ A/m^2. These simulations were produced using Vaughan's SEY model, where parameters for copper are chosen as $E_{max0} = 277.5$ eV, $\delta_{max0} = 2.088$.[59]

As the FWHM decreases, $|t_{max,gauss}|$ and $\theta_{m,gauss}$ increase and the susceptibility band becomes wider [Fig. 5(c)].

In Fig. 5, we also observe an extension of the susceptibility bands along the transverse axis ($f \times d -$ axis) with Gaussian-type electric field compared to those with sinusoidal electric fields. For instance, multipactor is not observed for $fd \lesssim 0.7$ GHz mm for sinusoidal rf operation [Fig. 5(a)]. However, for Gaussian-type rf operation, the first-order multipactor susceptibility band ($N = 1$) seems to be extended in the $fd \lesssim 0.7$ GHz mm region. To understand this, we recall that a Gaussian-type signal can be decomposed into multiple sinusoidal signals with different carrier frequencies (see the Appendix of Ref. 27 for details). Therefore, in the $fd \lesssim 0.7$ GHz mm region of Fig. 5, while the fundamental frequency component of the Gaussian-type electric field is incapable of developing multipactor, its higher frequency components might result in multipactor development. From another perspective, for a fixed rf period, the Gaussian-type electric field is less efficient for electron acceleration compared to the sinusoidal electric field.[27,61] Therefore, when the gap distance (d) is very small, sinusoidal rf fields fail to establish resonant electron motion as electrons emitted from one surface reach the other surface too early. On the other hand, Gaussian-type rf fields with the same fundamental rf frequency (f) can successfully establish resonant electron motion across the same gap distance because of the less efficient electron acceleration.

For sinusoidal rf operation [Fig. 5(a)], different multipactor modes (i.e., $N = 1, 3, \ldots$, etc.) result in distinct multipactor bands.[59] Distinct susceptibility bands are also observed for Gaussian-type rf operation with $\Delta\tau = 0.15T_{rf}$ [Fig. 5(b)]. Figures 7(a)–7(c) confirm that these separate bands represent different multipactor modes (see Fig. 5 of Ref. 59 for the detailed analysis of different multipactor modes and corresponding particle trajectories

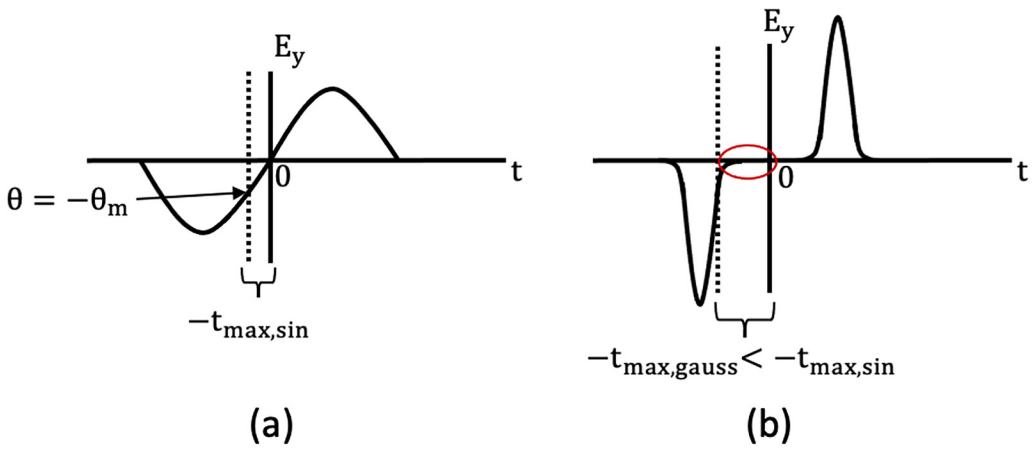

FIG. 6. (a) For sinusoidal rf operation, $\theta = -\theta_m$ corresponding to the upper boundary represents the earliest electron emission time, $-t_{max,sin}$. (b) For Gaussian-type rf operation, $|t_{max,gauss}| > |t_{max,sin}|$, resulting in an expansion of the susceptibility bands and an increase in the upper susceptibility boundary.

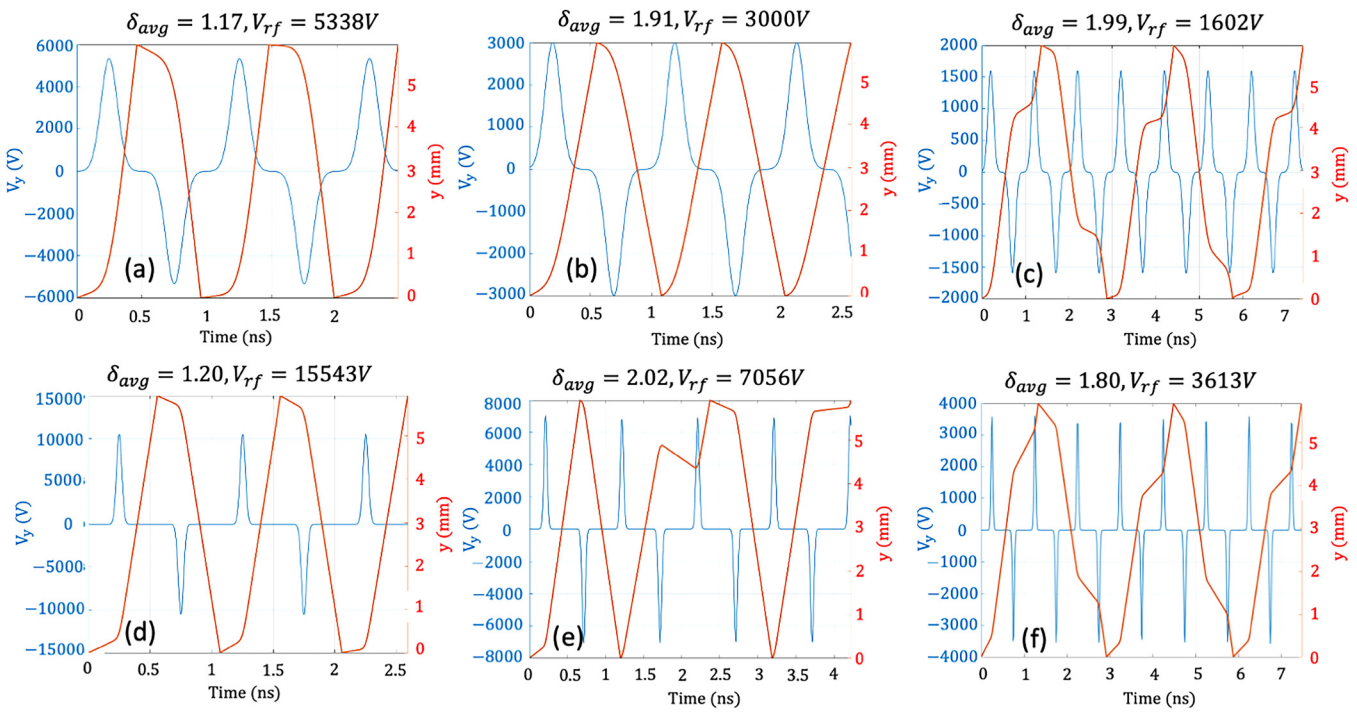

FIG. 7. Top row: Instantaneous rf voltage, $V_y = V_{rf}\{\exp[-\beta(t-t_1)^2] - \exp[\beta(t-t_2)^2]\}$, $nT_{rf} \le t < (n+1)T_{rf}$ (blue lines) and the corresponding macroparticle trajectories (red lines) obtained from MC simulation for $\Delta\tau = 0.15T_{rf}$ with (a) $V_{rf} = 5338$ V, (b) $V_{rf} = 3000$ V, and (c) $V_{rf} = 1602$ V. Bottom row: Instantaneous rf voltage (blue lines) and corresponding macroparticle trajectories (red lines) for $\Delta\tau = 0.05T_{rf}$ with (d) $V_{rf} = 15543$ V, (b) $V_{rf} = 7056$ V, (c) $V_{rf} = 3613$ V. For all the cases, we use fd = 5.92 GHz mm, fundamental rf frequency, f = 1 GHz. Plots (a)–(c) correspond to points m, n, and o, in Fig. 5(b), respectively and plots (d)–(f) correspond to the points p, q, and r, in Fig. 5(c), respectively. The values of δ_{avg} are calculated from the MC simulation as described in Sec. III A. These simulations were produced using Vaughan's SEY model, where parameters for copper are chosen as $E_{max0} = 277.5$ eV, $\delta_{max0} = 2.088$.[59]

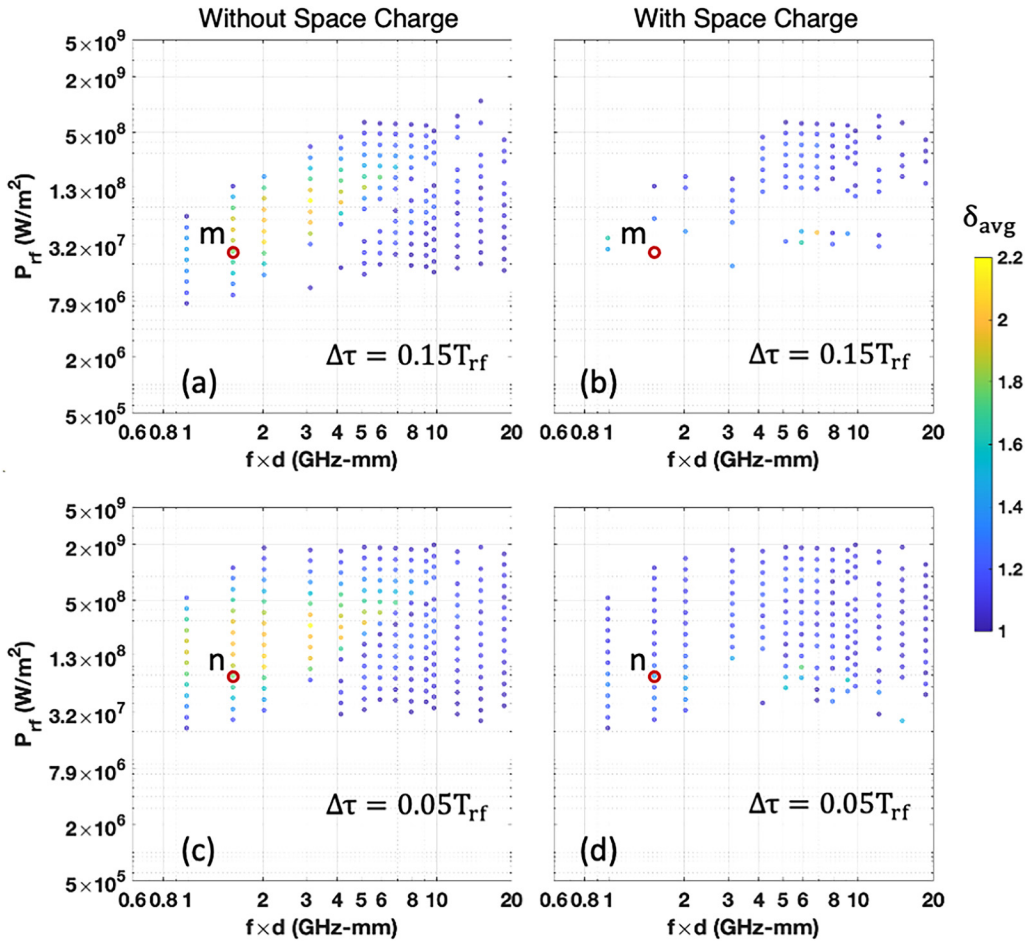

FIG. 8. Multipactor susceptibility charts in the $V_{rf} - fd$ space calculated from CST simulation; top row: For $\Delta\tau = 0.15T_{rf}$, (a) without space-charge effects (no volume space charge and no image charge field) and (b) with space-charge effects. Bottom row: for $\Delta\tau = 0.05T_{rf}$, (c) without space-charge effects and (d) with space-charge effects. Color bar shows the time averaged secondary electron yield, δ_{avg}, calculated from the CST simulations as described in Sec. III B. For all the cases, we use rf repetition period, $T_{rf} = 1$ ns, and the variation in fd is obtained by varying the gap distance, d. We use the number of electrons contained in each particle, $N_e = 5 \times 10^5$, emission period of seed particles, $t_{emission} = 1$ ns and the total number of seed particles, $N_{seed,total} = 1515$ corresponding to an initial seed current density, $J_{seed} = 12.15 \times 10^8$ A/m^2. These simulations were produced using Vaughan's SEY model, where parameters for copper are chosen as $E_{max0} = 277.5$ eV, $\delta_{max0} = 2.088$.[59]

with sinusoidal rf fields). We observe that for $(fd, V_{rf}) \sim (5.92\,\text{GHz mm}, 5338\,\text{V})$ [Fig. 7(a)] and $(5.92\,\text{GHz mm}, 3000\,\text{V})$ [Fig. 7(b)], the transit time of the macroparticle from the bottom plate to the top plate ($\tau_{A\to B}$) and the transit time from the top plate to the bottom plate ($\tau_{B\to A}$) are approximately $\frac{T_{rf}}{2} = 0.5$ ns, as indicated by Fig. 1. Therefore, the corresponding (fd, V_{rf}) points (m and n, respectively) lie inside the first susceptibility band of Fig. 5(b) (i.e., multipactor mode, N = 1). For $(fd, V_{rf}) \sim (5.92\,\text{GHz mm}, 1602\,\text{V})$ [Fig. 7(c)], $\tau_{A\to B} = \tau_{B\to A} \approx \frac{3T_{rf}}{2} = 1.5$ ns. Therefore, the corresponding (fd, V_{rf}) point o lies inside the second susceptibility band of Fig. 5(b) (i.e., multipactor mode, N = 3).

For Gaussian-type rf operation with $\Delta\tau = 0.05T_{rf}$ [Fig. 5(c)], the susceptibility bands are found to be partially overlapped. In this overlapping region, mixed multipactor modes are observed, where $\tau_{A\to B} \neq \tau_{B\to A}$. Figure 7(e) [corresponding to point q in Fig. 5(c)] shows such a mixed multipactor mode for $(fd, V_{rf}) \sim (5.92\,\text{GHz mm}, 7056\,\text{V})$. Points p and r in Fig. 5(c) represent pure multipactor modes N = 1 and 3, respectively, for $\Delta\tau = 0.05T_{rf}$, as can be observed from their corresponding macroparticle trajectories in Figs. 7(d) and 7(f), respectively.

Next, we turn on the function of space-charge effects in CST[59,68,70] and examine multipactor susceptibility and its time dependent dynamics. When the function of space-charge effects is turned on in CST, the simulations account for volume space charge as well as the image charge field, which are not accounted for in simulations when the function is turned off.

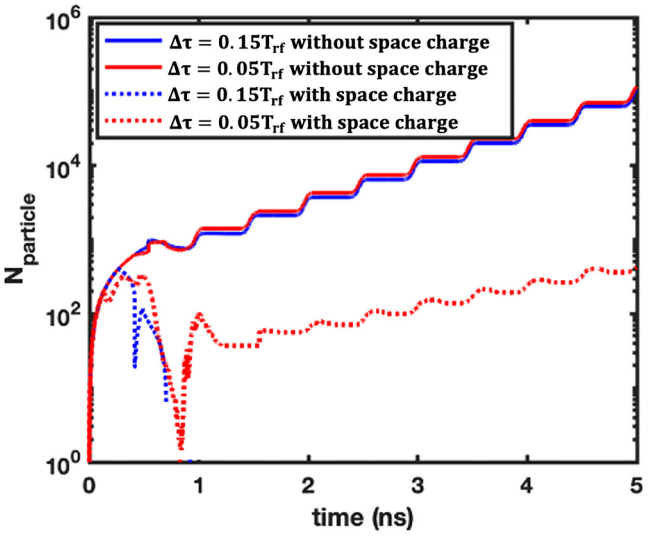

FIG. 9. Evolution of the particle population ($N_{particle}$) for $\Delta\tau = 0.15T_{rf}$ without space charge [corresponding to point m in Fig. 8(a)], $\Delta\tau = 0.05T_{rf}$ without space charge [corresponding to point n in Fig. 8(c)], $\Delta\tau = 0.15T_{rf}$ with space charge [corresponding to point m in Fig. 8(b)], and $\Delta\tau = 0.05T_{rf}$ with space charge [corresponding to point n in Fig. 8(d)]. For all cases, we use $T_{rf} = 1$ ns and d = 1.52 mm. Note that points m and n represent a time averaged rf power per unit area, $P_{rf} = 2.7 \times 10^7$ and 7.9×10^7 W/m^2, respectively. Also note that for the chosen P_{rf} values and without space charge, average secondary electron yield and particle growth rate for $\Delta\tau = 0.15T_{rf}$ (solid blue curve) and $\Delta\tau = 0.05T_{rf}$ (solid red curve) are similar. However, with space charge, multipactor is suppressed for $\Delta\tau = 0.15T_{rf}$ (dotted blue curve), whereas for $\Delta\tau = 0.05T_{rf}$ (dotted red curve), multipactor discharge is present. These simulations were produced using Vaughan's SEY model, where parameters for copper are chosen as $E_{max0} = 277.5$ eV, $\delta_{max0} = 2.088$.[59]

We observe that for an initial seed current density, $J_{seed} = 12.15 \times 10^8$ A/m^2, space charge effects result in a shrinkage of multipactor susceptibility bands for $\Delta\tau = 0.15T_{rf}$ [Fig. 8(b)]. However, for $\Delta\tau = 0.05T_{rf}$, the effect of space charge on multipactor susceptibility is not prominent [Fig. 8(d)] with the same seed current density. The average SEY is reduced in Fig. 8(d) compared to Fig. 8(c), while the susceptibility bands in Figs. 8(c) and 8(d) remain relatively unchanged.

Figure 9 shows the evolution of the particle population with (dotted lines) and without (solid lines) space charge for $(\Delta\tau, P_{rf}, V_{rf}) \sim (0.15T_{rf}, 2.7 \times 10^7$ W/m^2, 323 V) [blue lines in Fig. 9, corresponding to point m in Figs. 8(a) and 8(b)] and $(\Delta\tau, P_{rf}, V_{rf}) \sim (0.05T_{rf}, 7.9 \times 10^7$ W/m^2, 947 V) [red lines in Fig. 9, corresponding to point n in Figs. 8(c) and 8(d)]. These P_{rf} values are so chosen that the particle growth rate and, therefore, the time averaged SEY without space charge for $\Delta\tau = 0.15T_{rf}$ and $0.05T_{rf}$ are similar (solid curves in Fig. 9). However, we observe that when space charge is turned on, multipactor is completely suppressed for $\Delta\tau = 0.15T_{rf}$ (dotted blue curve in Fig. 9), whereas for $\Delta\tau = 0.05T_{rf}$ (dotted red curve in Fig. 9), multipactor discharge is present with a lower SEY than the solid curves.

We then investigate the (y, v_y) phase space of the electrons in the gap for different FWHMs of the Gaussian profile of the rf field to understand why the effect of space charge is more prominent on multipactor susceptibility for a larger FWHM.

For the CST simulation with 1 GHz excitation, the particle source at the top plate emits seed particles into the vacuum gap during the first period of the excitation ($t_{emission} = 1$ ns) at a constant rate of 1515 particles/ns. Therefore, from t = 0 to t = 0.30 ns, 454 seed particles are emitted into the vacuum gap. As shown in panel A of Fig. 10, when space-charge is accounted for, some of these seed particles are re-absorbed by the top surface due to the virtual cathode effect (i.e., the formation of space charge potential minimum to reflect electrons)[59,66,71–74] and the number of particles at t = 0.30 ns for $\Delta\tau = 0.15T_{rf}$ and $0.05T_{rf}$ are 372 and 319, respectively.

As seed charge density grows, the virtual cathode effect becomes stronger. As a result, at t = 0.40 ns (panel B of Fig. 10), we observe that space charge causes the velocity reversal of particles [red circled region in Figs. 10(b) and 10(g)]. From Fig. 11, we observe that at t = 0.40 ns, the instantaneous rf electric field (E_y) becomes almost zero for $\Delta\tau = 0.05T_{rf}$ (red curve in Fig. 11). As a result, the velocity reversal due to the virtual cathode effect is more prominent in Fig. 10(g) compared in Fig. 10(b). As the velocity of the impacting particles is very high [approximately 116 eV impact energy, shown in the red circled region in Fig. 10(g)], they generate secondary particles through secondary electron emission. Such secondary electron emission is not observed in Fig. 10(b) as the impact velocity is quite low (approximately 8 eV impact energy) in this case [red circled region in Fig. 10(b)] due to a higher value of the rf electric field (E_y) (blue curve in Fig. 11). As a result, at t = 0.50 ns, the number of particles for $\Delta\tau = 0.05T_{rf}$ is much higher [312 in Fig. 10(h)] than that for $\Delta\tau = 0.15T_{rf}$ [98 in Fig. 10(c)].

For 0.50 ns < t < 1.00 ns, the rf field is reversed. Therefore, during this period, the particles generated during the positive half cycle (i.e., 0 ns < t < 0.50 ns) impact and get absorbed by the top plate. We observe from panel D of Fig. 10 that at t = 0.65 ns, all the seed particles are absorbed by the top plate for $\Delta\tau = 0.15T_{rf}$. However, at t = 0.90 ns, some seed particles still remain in the vacuum gap for $\Delta\tau = 0.05T_{rf}$ [Fig. 10(j)]. These remaining seed particles result in multipactor discharge during the next rf periods (as shown in the dotted red curve of Fig. 9).

Wen *et al.* showed[27] that when a dielectric surface is exposed to a Gaussian-type electric field, the single-surface multipactor strength at saturation is reduced compared to a sinusoidal electric field. Figure 12(a) shows that the two-surface multipactor strength, i.e., the electron population (n_e) at multipactor saturation, can also be reduced with Gaussian-type rf operation. We observe from Figs. 12(a) and 12(b) that the multipactor strength decreases as the FWHM of the Gaussian-type rf field decreases. We find that for Gaussian-type rf operation with $\Delta\tau = 0.05T_{rf}$ [leftmost points in Fig. 12(b)], first-order (N = 1) multipactor strength [black curves in Fig. 12(b)] is reduced by almost 50% and third-order (N = 3) multipactor strength [red curves in Fig. 12(b)] is reduced by almost 90% compared to the sinusoidal rf operation with the same time averaged rf power per unit area.

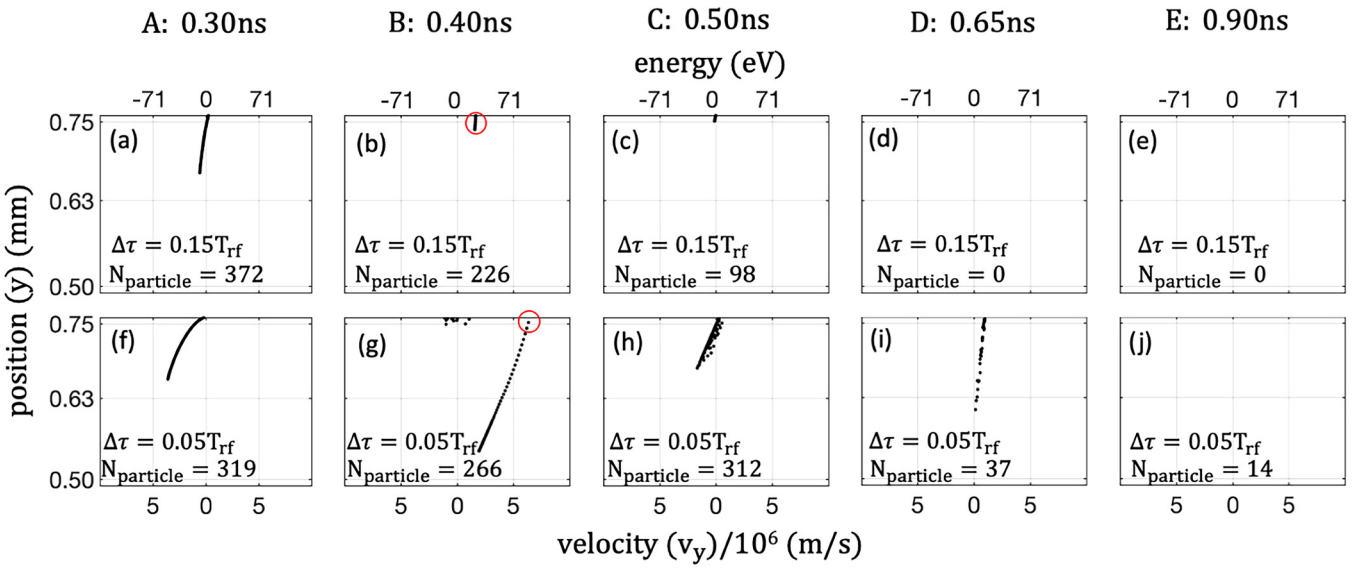

FIG. 10. y vs v_y with space charge for (a)–(e) $(\Delta\tau, P_{rf}, V_{rf}) \sim (0.15T_{rf}, 2.7 \times 10^7\,W/m^2, 323\,V)$ and (f)–(j) $(\Delta\tau, P_{rf}, V_{rf}) \sim (0.05T_{rf}, 7.9 \times 10^7\,W/m^2, 947\,V)$, at times t = 0.30 ns (vertical panel A), 0.40 ns (vertical panel B), 0.50 ns (vertical panel C), 0.65 ns, (vertical panel D), and 0.90 ns, (vertical panel E), where $T_{rf} = 1$ ns, f = 1 GHz, d = 1.52 mm, i.e., fd = 1.52 GHz mm. Note that the plots have two x axes: the bottom x axis shows the velocity (v_y) and the top x axis shows the corresponding energy of the particles. In all plots, y = 0.76 and y = −0.76 mm correspond to the top surface and the bottom surface of the two-surface geometry. The plots have been zoomed in the region near the top plate for better visualization of particles, which are close to the top plate. The total number of seed particles in the simulation is set as $N_{seed,total} = 1515$, and the number of electrons contained in each particle $N_e = 5 \times 10^5$, resulting in a seed current density, $J_{seed} = 12.15 \times 10^8\,A/m^2$. These simulations were produced using Vaughan's SEY model, where parameters for copper are chosen as $E_{max0} = 277.5$ eV, $\delta_{max0} = 2.088$.[59]

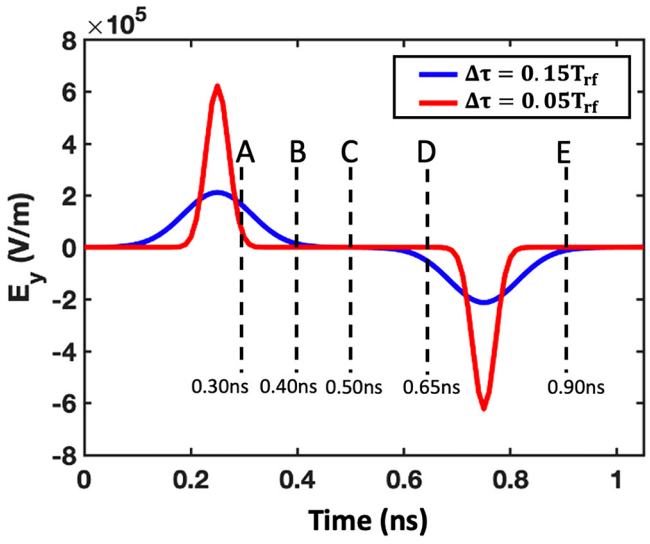

FIG. 11. The instantaneous electric field of the Gaussian form for $(\Delta\tau, P_{rf}, V_{rf}) \sim (0.15T_{rf}, 2.7 \times 10^7\,W/m^2, 323\,V)$ (solid blue curve) and $(\Delta\tau, P_{rf}, V_{rf}) \sim (0.05T_{rf}, 7.9 \times 10^7\,W/m^2, 947\,V)$ (solid red curve), where $T_{rf} = 1$ ns. Dashed vertical lines A, B, C, D, and E correspond to the vertical panels of Fig. 10 from left to right, respectively.

V. CONCLUSIONS

We investigated two surface multipactor with Gaussian-type rf fields using Monte Carlo simulation and the CST particle-in-cell code. We observed that multipactor susceptibility is sensitive to the FWHM of the Gaussian profile. As the FWHM of the Gaussian profile decreases, the threshold peak rf voltage and the threshold rf power for multipactor increase. In addition, multipactor susceptibility bands become wider for Gaussian-type RF operation compared to the sinusoidal RF operation.

CST PIC simulation with space-charge effects reveals that for a large FWHM of the Gaussian profile, a high initial seed current density can result in a shrinkage of the multipactor susceptibility bands. However, as the FWHM decreases, the effect of space charge on multipactor susceptibility becomes less prominent. The multipactor strength, i.e., the electron population at multipactor saturation, can be significantly reduced with a Gaussian-type electric field with small FWHM compared to a sinusoidal electric field.

Future work may include the development of an analytical theory for Gaussian-type rf field induced two-surface multipactor and validation of presented results against experiments as well as investigating other waveforms, especially those created with a small number of sinusoidal carriers, as practical possibilities. Non-sinusoidal rf induced two-surface multipactor in other geometries, such as microstrip, circular, and coaxial waveguides might also be of interest. In addition, the scaling of the V–fd relationship

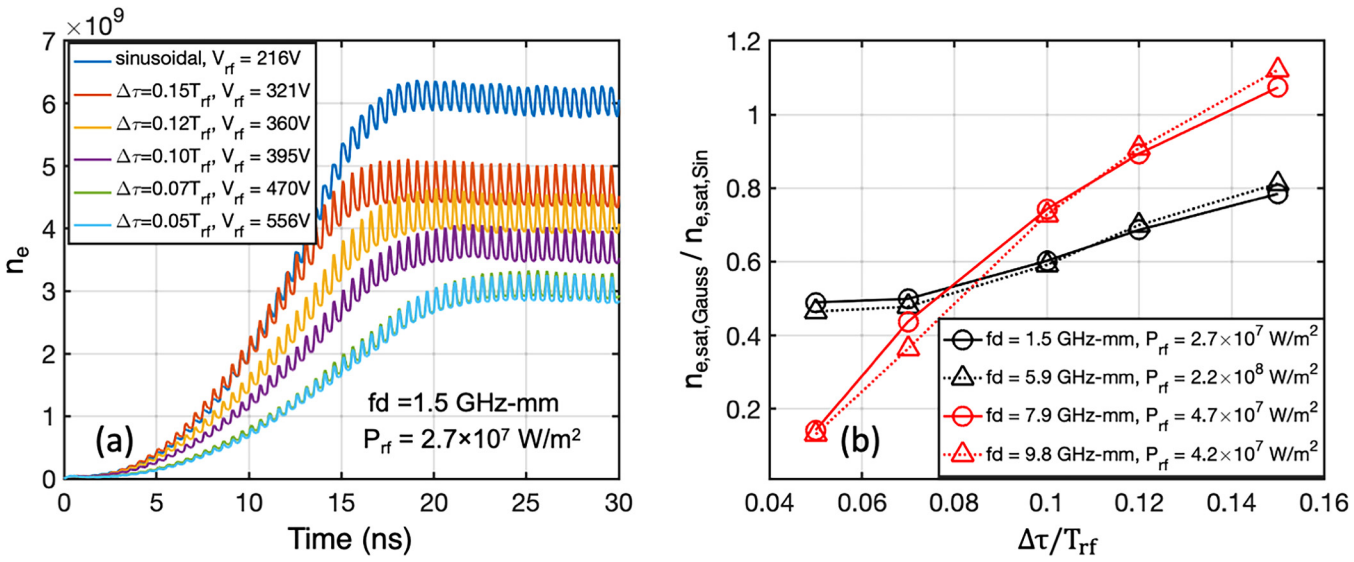

FIG. 12. (a) Evolution of the electron population, n_e, in the CST simulation with space charge effect for sinusoidal electric field and Gaussian-type electric field with different FWHMs at (fd, P_{rf}) ~ (1.5 GHz mm, 2.7×10^7 W/m^2). (b) The electron population at saturation with Gaussian-type electric fields ($n_{e,sat,Gauss}$) with different FWHM values and at different (fd, P_{rf}) points, normalized to the electron population at saturation with a sinusoidal electric field ($n_{e,sat,Sin}$) with the same P_{rf} as the Gaussian-type electric fields. We use the number of electrons contained in each computer particle, $N_e = 10^5$, emission period of seed particles, $t_{emission} = 1$ ns and the total number of seed particles, $N_{seed,total} = 1515$ corresponding to an initial seed current density, $J_{seed} = 2.43 \times 10^8$ A/m^2. These simulations were produced using Vaughan's SEY model, where parameters for copper are chosen as $E_{max0} = 277.5$ eV, $\delta_{max0} = 2.088$.[59]

due to effects such as varying the rf frequency beyond the electron plasma frequency, presence of magnetic fields, relativistic speeds and varying mass (e.g., ions or anions) of particles, and collisions between the particles, can be explored. The effects due to the presence of background gas may also be explored,[31] along with the transition from multipactor to ionization breakdown.[75–77]

ACKNOWLEDGMENTS

This work was supported by the Air Force of Scientific Research (AFOSR) MURI under Grant Nos. FA9550-18-1-0062 and FA9550-21-1-0367.

AUTHOR DECLARATIONS

Conflict of Interest

The authors have no conflicts to disclose.

Author Contributions

Asif Iqbal: Conceptualization (equal); Formal analysis (equal); Investigation (equal); Methodology (equal); Validation (equal); Visualization (equal); Writing – original draft (lead); Writing – review & editing (equal). **De-Qi Wen:** Conceptualization (equal); Formal analysis (equal); Investigation (equal); Methodology (equal); Validation (equal); Visualization (equal); Writing – original draft (equal); Writing – review & editing (equal). **John Verboncoeur:** Conceptualization (equal); Formal analysis (equal); Funding acquisition (lead); Investigation (equal); Methodology (equal); Supervision (equal); Writing – review & editing (equal). **Peng Zhang:** Conceptualization (equal); Formal analysis (equal); Funding acquisition (equal); Investigation (equal); Methodology (equal); Supervision (lead); Validation (equal); Visualization (equal); Writing – review & editing (equal).

DATA AVAILABILITY

The data that support the findings of this study are available from the corresponding author upon reasonable request.

REFERENCES

[1]P. T. Farnsworth, "Television by electron image scanning," J. Frankl. Inst. **218**(4), 411–444 (1934).
[2]J. R. M. Vaughan, "Multipactor," IEEE Trans. Electron Devices **35**(7), 1172–1180 (1988).
[3]R. A. Kishek, Y. Y. Lau, L. K. Ang, A. Valfells, and R. M. Gilgenbach, "Multipactor discharge on metals and dielectrics: Historical review and recent theories," Phys. Plasmas **5**(5), 2120–2126 (1998).
[4]R. A. Kishek, "Interaction of multipactor discharge and rf structures," Ph.D. (University of Michigan, Michigan, United States, 1997).
[5]A. Valfells, "Multipactor discharge: Frequency response, suppression, and relation to window breakdown," Ph.D. (University of Michigan, Michigan, United States, 2000).
[6]A. Iqbal, D.-Q. Wen, J. Verboncoeur, and P. Zhang, "Recent advances in multipactor physics and mitigation," High Voltage (published online, 2023).
[7]J. Benford, J. A. Swegle, and E. Schamiloglu, *High Power Microwaves*, 3rd ed. (CRC Press, 2015).

[8]S. A. Rice, "Multipactor in the presence of higher-order modes: A numerical study," Ph.D. (Michigan State University, 2017).
[9]O. Bruning *et al.*, "Electron cloud and beam scrubbing in the LHC," in *Proceedings of the 1999 Particle Accelerator Conference (Cat. No.99CH36366)*, New York, NY, USA (IEEE, 1999), Vol. 4, pp. 2629–2631.
[10]S. Y. Zhang, M. Blaskiewicz, H. C. Hseuh, and J. Wei, "Beam scrubbing strategy for electron-cloud suppression in the spallation neutron source ring," in *Proceedings of the 2003 Bipolar/BiCMOS Circuits and Technology Meeting (IEEE Cat. No.03CH37440)*, Portland, OR, USA (IEEE, 2003), pp. 3419–3421.
[11]P. Wong, P. Zhang, and J. Luginsland, "Recent theory of traveling-wave tubes: A tutorial-review," Plasma Res. Express **2**(2), 023001 (2020).
[12]D. Gonzalez-Iglesias *et al.*, "Novel multipactor studies in RF satellite payloads: Single-carrier digital modulated signals and ferrite materials," in *2017 IEEE MTT-S International Conference on Numerical Electromagnetic and Multiphysics Modeling and Optimization for RF, Microwave, and Terahertz Applications (NEMO)*, Seville, Spain (IEEE, 2017), pp. 248–250.
[13]S. K. Nagesh, D. Revannasiddiah, and S. V. K. Shastry, "Investigation of multipactor breakdown in communication satellite microwave co-axial systems," Pramana **64**(1), 95–110 (2005).
[14]T. P. Graves, A. A. Hubble, and P. T. Partridge, "Physics-based standard for RF breakdown prevention in spacecraft components," in 2016 *IEEE International Conference on Plasma Science (ICOPS)* (IEEE, 2016), p. 1.
[15]J. Hillairet, M. Goniche, N. Fil, M. Belhaj, and J. Puech, "Multipactor in high power radio-frequency systems for nuclear fusion," arXiv (2017).
[16]D. H. Preist and R. C. Talcott, "On the heating of output windows of microwave tubes by electron bombardment," IRE Trans. Electron Devices **8**(4), 243–251 (1961).
[17]J. R. M. Vaughan, "Some high-power window failures," IRE Trans. Electron Devices **8**(4), 302–308 (1961).
[18]S. Yamaguchi, Y. Saito, S. Anami, and S. Michizono, "Trajectory simulation of multipactoring electrons in an S-band pillbox RF window," IEEE Trans. Nucl. Sci. **39**(2), 278–282 (1992).
[19]A. Neuber, J. Dickens, D. Hemmert, H. Krompholz, L. L. Hatfield, and M. Kristiansen, "Window breakdown caused by high-power microwaves," IEEE Trans. Plasma Sci. **26**(3), 296–303 (1998).
[20]P. Y. Wong, Y. Y. Lau, P. Zhang, N. Jordan, R. M. Gilgenbach, and J. Verboncoeur, "The effects of multipactor on the quality of a complex signal propagating in a transmission line," Phys. Plasmas **26**(11), 112114 (2019).
[21]T. P. Graves, "Experimental investigation of electron multipactor discharges at very high frequency," Ph.D. (Massachusetts Institute of Technology, 2006).
[22]A. Iqbal, "Multipactor discharge with two-frequency RF fields," Ph.D. (Michigan State University, Michigan, United States, 2021).
[23]H. Bruining, J. H. De Boer, and W. G. Burgers, "Secondary electron emission of soot in valves with oxidecathode," Physica **4**, 267–275 (1937).
[24]A. J. Dekker, "Secondary electron emission," in *Solid State Physics: Advances in Research and Applications*, edited by F. Seitz, and D. Turnbull (Academic Press, 1958), Vol. 6, pp. 251–311.
[25]J. R. M. Vaughan, "A new formula for secondary emission yield," IEEE Trans. Electron Devices **36**(9), 1963–1967 (1989).
[26]M. Furman and M. Pivi, "Probabilistic model for the simulation of secondary electron emission," Phys. Rev. Spec. Top. Accel. Beams **5**(12), 124404 (2002).
[27]D.-Q. Wen, A. Iqbal, P. Zhang, and J. P. Verboncoeur, "Suppression of single-surface multipactor discharges due to non-sinusoidal transverse electric field," Phys. Plasmas **26**(9), 093503 (2019).
[28]R. A. Kishek and Y. Y. Lau, "Multipactor discharge on a dielectric," Phys. Rev. Lett. **80**(1), 193 (1998).
[29]L. K. Ang, Y. Y. Lau, R. A. Kishek, and R. M. Gilgenbach, "Power deposited on a dielectric by multipactor," IEEE Trans. Plasma Sci. **26**(3), 290–295 (1998).
[30]A. Iqbal, P. Y. Wong, D.-Q. Wen, S. Lin, J. Verboncoeur, and P. Zhang, "Time-dependent physics of single-surface multipactor discharge with two carrier frequencies," Phys. Rev. E **102**(4), 043201 (2020).
[31]P. Zhang, Y. Y. Lau, M. Franzi, and R. M. Gilgenbach, "Multipactor susceptibility on a dielectric with a bias dc electric field and a background gas," Phys. Plasmas **18**(5), 053508 (2011).
[32]C. Y. Vallgren *et al.*, "Amorphous carbon coatings for the mitigation of electron cloud in the CERN super proton synchrotron," Phys. Rev. Spec. Top. Accel. Beams **14**(7), 071001 (2011).
[33]J. Eldred, M. Backfish, S. Kato, C.-Y. Tan, and R. Zwaska, "Beam tests of diamond-like carbon coating for mitigation of electron cloud," in *Presented at the 8th Int. Particle Accelerator Conf. (IPAC'17)*, Copenhagen, Denmark (JACoW, 2017), pp. 4497–4500.
[34]H. K. A. Nguyen, J. Mankowski, J. C. Dickens, A. A. Neuber, and R. P. Joshi, "Calculations of secondary electron yield of graphene coated copper for vacuum electronic applications," AIP Adv. **8**(1), 015325 (2018).
[35]J. Yang, W. Cui, G. Xie, Y. Bao, M. Ye, and Q. Song, "Nanofabrication techniques used for suppressing multipactor in space applications," in *2018 IEEE International Conference on Manipulation, Manufacturing and Measurement on the Nanoscale (3M-NANO)*, Hangzhou, China (IEEE, 2018), pp. 241–244.
[36]J. Wang, Y. Wang, Y. Xu, Y. Zhang, B. Zhang, and W. Wei, "Secondary electron emission characteristics of graphene films with copper substrate*," Chin. Phys. C **40**(11), 117003 (2016).
[37]G. Feng *et al.*, "Gas desorption and secondary electron emission from graphene coated copper due to E-beam stimulation," Coatings **13**(2), 370 (2023).
[38]D. Wu *et al.*, "Fabrication of porous Ag/TiO2/Au coatings with excellent multipactor suppression," Sci. Rep. **7**(1), 1 (2017).
[39]C. Chang *et al.*, "Field distribution, HPM multipactor, and plasma discharge on the periodic triangular surface," Laser Part. Beams **28**(1), 185–193 (2010).
[40]V. Nistor *et al.*, "Multipactor suppression by micro-structured gold/silver coatings for space applications," Appl. Surf. Sci. **315**, 445–453 (2014).
[41]C. Watts, M. Gilmore, and E. Schamiloglu, "Effects of laser surface modification on secondary electron emission of copper," IEEE Trans. Plasma Sci. **39**(3), 836–841 (2011).
[42]S. Zhang, G.-Y. Sun, H.-B. Mu, B.-P. Song, J. Xue, and G.-J. Zhang, "Modelling vacuum flashover mitigation with complex surface microstructure: Mechanism and application," High Volt. **5**(2), 110–121 (2020).
[43]M. Pivi, F. K. King, R. E. Kirby, T. O. Raubenheimer, G. Stupakov, and F. L. Pimpec, "Sharp reduction of the secondary electron emission yield from grooved surfaces," J. Appl. Phys. **104**(10), 104904 (2008).
[44]J. M. Sattler, R. A. Coutu, R. Lake, T. Laurvick, T. Back, and S. Fairchild, "Modeling micro-porous surfaces for secondary electron emission control to suppress multipactor," J. Appl. Phys. **122**(5), 055304 (2017).
[45]A. Iqbal *et al.*, "Empirical modeling and Monte Carlo simulation of secondary electron yield reduction of laser drilled microporous gold surfaces," J. Vac. Sci. Technol., B **38**(1), 013801 (2020).
[46]J. Ludwick *et al.*, "Angular dependence of secondary electron yield from microporous gold surfaces," J. Vac. Sci. Technol., B **38**(5), 054001 (2020).
[47]M. Mirmozafari, A. Iqbal, P. Zhang, N. Behdad, J. H. Booske, and J. P. Verboncoeur, "Secondary electron yield characterization of high porosity surfaces for multipactor-free microwave components," Phys. Plasmas **29**(8), 082109 (2022).
[48]M. Ye *et al.*, "Suppression of secondary electron yield by micro-porous array structure," J. Appl. Phys. **113**(7), 074904 (2013).
[49]X. Yang *et al.*, "Design and 3D printing of porous cavity insulation structure for ultra-high electrical withstanding capability," High Volt. **8**(4), 717–727 (2023).
[50]O. A. Ivanov, M. A. Lobaev, V. A. Isaev, and A. L. Vikharev, "Suppressing and initiation of multipactor discharge on a dielectric by an external dc bias," Phys. Rev. Spec. Top. - Accel. Beams **13**(2), 022004 (2010).
[51]C. Chang, G. Liu, C. Tang, C. Chen, and J. Fang, "Review of recent theories and experiments for improving high-power microwave window breakdown thresholds," Phys. Plasmas **18**(5), 055702 (2011).
[52]A. Valfells, L. K. Ang, Y. Y. Lau, and R. M. Gilgenbach, "Effects of an external magnetic field, and of oblique radio-frequency electric fields on multipactor discharge on a dielectric," Phys. Plasmas **7**(2), 750–757 (2000).

[53]C. Chang, G. Z. Liu, C. X. Tang, C. H. Chen, H. Shao, and W. H. Huang, "Suppression of high-power microwave dielectric multipactor by resonant magnetic field," Appl. Phys. Lett. **96**(11), 111502 (2010).
[54]C. Chang, J. Fang, Z. Zhang, C. Chen, C. Tang, and Q. Jin, "Experimental verification of improving high-power microwave window breakdown thresholds by resonant magnetic field," Appl. Phys. Lett. **97**(14), 141501 (2010).
[55]A. Iqbal, J. Verboncoeur, and P. Zhang, "Multipactor susceptibility on a dielectric with two carrier frequencies," Phys. Plasmas **25**(4), 043501 (2018).
[56]A. Iqbal, J. Verboncoeur, and P. Zhang, "Temporal multiparticle Monte Carlo simulation of dual frequency single surface multipactor," Phys. Plasmas **26**(2), 024503 (2019).
[57]A. Iqbal, P. Y. Wong, J. P. Verboncoeur, and P. Zhang, "Frequency-domain analysis of single-surface multipactor discharge with single- and dual-tone RF electric fields," IEEE Trans. Plasma Sci. **48**(6), 1950–1958 (2020).
[58]A. Iqbal, P. Y. Wong, D.-Q. Wen, J. P. Verboncoeur, and P. Zhang, "A review of recent studies on two-frequency RF field-induced single-surface multipactor discharge," IEEE Trans. Plasma Sci. **49**(11), 3284–3292 (2021).
[59]A. Iqbal, J. Verboncoeur, and P. Zhang, "Two surface multipactor discharge with two-frequency rf fields and space-charge effects," Phys. Plasmas **29**(1), 012102 (2022).
[60]V. Semenov, A. Kryazhev, D. Anderson, and M. Lisak, "Multipactor suppression in amplitude modulated radio frequency fields," Phys. Plasmas **8**(11), 5034–5039 (2001).
[61]D.-Q. Wen, A. Iqbal, P. Zhang, and J. P. Verboncoeur, "Susceptibility of multipactor discharges near a dielectric driven by a Gaussian-type transverse rf electric field," Appl. Phys. Lett. **121**(16), 164103 (2022).
[62]M. Mirmozafari, N. Behdad, and J. Booske, "Multipactor suppression using multitone signals," in *2022 IEEE International Conference on Plasma Science (ICOPS)* (IEEE, 2022), pp. 1–2.
[63]D.-Q. Wen, P. Zhang, Y. Fu, J. Krek, and J. P. Verboncoeur, "Temporal single-surface multipactor dynamics under obliquely incident linearly polarized electric field," Phys. Plasmas **26**(12), 123509 (2019).
[64]G. Romanov, "Simulation of multipacting with space charge effect," American J. Phys. and Applications **5**(6), 99–105 (2017).
[65]A. Valfells, J. P. Verboncoeur, and Y. Y. Lau, "Space-charge effects on multipactor on a dielectric," IEEE Trans. Plasma Sci. **28**(3), 529–536 (2000).
[66]P. Zhang, Y. S. Ang, A. L. Garner, Á. Valfells, J. W. Luginsland, and L. K. Ang, "Space–charge limited current in nanodiodes: Ballistic, collisional, and dynamical effects," J. Appl. Phys. **129**(10), 100902 (2021).
[67]Á. Coves, G. Torregrosa-Penalva, C. Vicente, B. Gimeno, and V. E. Boria, "Multipactor discharges in parallel-plate dielectric-loaded waveguides including space-charge effects," IEEE Trans. Electron Devices **55**(9), 2505–2511 (2008).
[68]CST Studio Suite, *Dassault Systems* (Vélizy-Villacoublay, France, 2019).
[69]J. R. M. Vaughan, "Secondary emission formulas," IEEE Trans. Electron Devices **40**(4), 830 (1993).
[70]S. V. Langellotti, N. M. Jordan, Y. Y. Lau, and R. M. Gilgenbach, "CST particle studio simulations of coaxial multipactor and comparison with experiments," IEEE Trans. Plasma Sci. **48**(6), 1942–1949 (2020).
[71]Á. Valfells, D. W. Feldman, M. Virgo, P. G. O'Shea, and Y. Y. Lau, "Effects of pulse-length and emitter area on virtual cathode formation in electron guns," Phys. Plasmas **9**(5), 2377–2382 (2002).
[72]W. Li, J. X. Ma, J. Li, Y. Zheng, and M. Tan, "Measurement of virtual cathode structures in a plasma sheath caused by secondary electrons," Phys. Plasmas **19**(3), 030704 (2012).
[73]J. W. Luginsland, S. McGee, and Y. Y. Lau, "Virtual cathode formation due to electromagnetic transients," IEEE Trans. Plasma Sci. **26**(3), 901–904 (1998).
[74]P. Zhang, Á. Valfells, L. K. Ang, J. W. Luginsland, and Y. Y. Lau, "100 years of the physics of diodes," Appl. Phys. Rev. **4**(1), 011304 (2017).
[75]D.-Q. Wen, P. Zhang, J. Krek, F. Yangyang, and J. P. Verboncoeur, "Parametric studies of stream instability-induced higher harmonics in plasma ionization breakdown near an emissive dielectric surface," Plasma Sources Sci. Technol. **31**(9), 095004 (2022).
[76]D.-Q. Wen, P. Zhang, J. Krek, Y. Fu, and J. P. Verboncoeur, "Higher harmonics in multipactor induced plasma ionization breakdown near a dielectric surface," Phys. Rev. Lett. **129**(4), 045001 (2022).
[77]D.-Q. Wen, P. Zhang, J. Krek, Y. Fu, and J. P. Verboncoeur, "Observation of multilayer-structured discharge in plasma ionization breakdown," Appl. Phys. Lett. **119**(26), 264102 (2021).